Theoretical study of metal/silica interfaces: Ti, Fe, Cr and Ni on β-cristobalite

Jacopo Baima, Ha-Linh Thi Le, Jacek Goniakowski, Claudine Noguera, Alexey Koltsov, Jean-Michel Mataigne

▶ **To cite this version:**

Jacopo Baima, Ha-Linh Thi Le, Jacek Goniakowski, Claudine Noguera, Alexey Koltsov, et al.. Theoretical study of metal/silica interfaces: Ti, Fe, Cr and Ni on β-cristobalite. Physical Chemistry Chemical Physics, 2020, 22 (37), pp.21453-21462. 10.1039/D0CP03216F . hal-02985573

HAL Id: hal-02985573
https://hal.science/hal-02985573v1

Submitted on 2 Nov 2020

HAL is a multi-disciplinary open access archive for the deposit and dissemination of scientific research documents, whether they are published or not. The documents may come from teaching and research institutions in France or abroad, or from public or private research centers.

L'archive ouverte pluridisciplinaire **HAL**, est destinée au dépôt et à la diffusion de documents scientifiques de niveau recherche, publiés ou non, émanant des établissements d'enseignement et de recherche français ou étrangers, des laboratoires publics ou privés.

PCCP

ARTICLE TYPE

Cite this: DOI: 00.0000/xxxxxxxxxx

Theoretical study of metal/silica interfaces: Ti, Fe, Cr and Ni on β-cristobalite

Jacopo Baima,[ab] Ha-Linh Thi Le,[ab] Jacek Goniakowski,*[a] Claudine Noguera,[a] Alexey Koltsov,[b] and Jean-Michel Mataigne[b]

Received Date
Accepted Date

DOI: 00.0000/xxxxxxxxxx

The understanding of interfacial effects and adhesion at oxide-metal contacts is of key importance in modern technology. Metal-silica interfaces specifically are relevant in electronics, catalysis and nanotechnology. However, adhesion at these interfaces is hindered by a formation of siloxane rings on the silica surface which saturate the dangling bonds at stoichiometric terminations. In this context, we report a thorough density functional theory study of the interaction between β-cristobalite and selected 3d transition metals under different oxygen conditions. For any given interface stoichiometry, we find a progressive decrease of the metal/silica interaction along the series, following the increase of metal electronegativity. Crucially, in presence of early transition metals (Ti or Cr) the surface siloxane rings are spontaneously broken, allowing for strong adhesion. Late transition metals interact only weakly with reconstructed surfaces, similarly to what was found for zinc. In absence of reconstruction, stoichiometric silica/metal contacts behave similarly to alumina/metal contacts, but display larger interactions across the interface. Based on these results, we show that early transition metal or stainless steel buffers can significantly improve the weak adhesion between silica and zinc, responsible for a poor performance of anti-corrosive galvanic zinc coatings on modern advanced high strength steels.

1 Introduction

Interaction of metals with oxide and glass substrates has been the subject of studies in the context of various applications, most prominently electronics and catalysis.[1–3] More recently, silica/metal interfaces have attracted renewed research attention, focused on novel applications such as strong metal support interaction (SMSI),[4–6] metal@SiO_2 core-shell nanoparticles,[7–10] and techniques for sintering control.[11,12] In addition, metal adhesion to silica and other large gap oxides has emerged as a key challenge for the steel-making industry, as light strengthening elements (Si, Al and Mn) used in modern advanced high strength steels (AHSS) are selectively oxidized during the recrystallization annealing process, with the oxides segregating to the steel surface.[13–19] In particular, quasi-continuous amorphous silica films can form, which dramatically reduces the adhesion of the zinc galvanic coatings routinely applied to enhance corrosion resistance.[14,17,20]

In this context, a microscopic understanding of the interface and adhesion properties of metal/silica junctions is essential. With respect to the large number of theoretical and *ab initio* studies dedicated to the adhesion of transition and noble metals on a variety of oxide surfaces[1,2,21–24], comparatively less results have been reported on metal/silica interfaces. Moreover, we are not aware of any systematic study of the interaction between silica and different metallic species. This may be due to the difficulty of using amorphous silica models in simulations due to their large size and structural inhomogeneity. In this respect, a strategy successfully adopted in the past consists of mimicking amorphous silica surfaces by those of one of its crystalline polymorphs, most commonly either α-quartz, or α- or β-cristobalite. While being an high-temperature polymorph, β-cristobalite has the advantage of having a density very close to that of amorphous silica.

Beyond the existing studies treating interfaces of different silica polymorphs with Cu, Ni, Al, Ag, and Pt,[25–33] we have recently analyzed zinc/β-cristobalite interfaces.[34] We have shown that the characteristics of the interface are very sensitive to the silica surface composition and structure. The stoichiometric terminations show a reconstruction which saturates all dangling bonds by forming two-membered siloxane rings, which have also been identified on dehydroxylated amorphous silica surfaces. While this strongly stabilizes the bare surfaces, it results in a very weak

[a] *CNRS and Sorbonne Université, UMR 7588, Institut des Nanosciences de Paris (INSP) 4 place Jussieu, 75005 Paris, France*
[b] *ArcelorMittal Maizières Research, voie Romaine, F-57280, Maizières lès Metz, France.*
* *E-mail: jacek.goniakowski@insp.jussieu.fr*

† Electronic Supplementary Information (ESI) available: additional structural, electronic structure, and interface energy images, and relaxed interface structures. See DOI: 10.1039/b000000x/

interaction with the zinc deposit, and explains the bad adhesion of anti-corrosive zinc coatings. Similar mechanisms related to to the saturation of surface dangling bonds have been shown to be crucial in explaining the sintering of silica-supported Pt clusters[30,31], as well as Cu/silica adhesion properties in electronic circuits[26] and ion release by coated silver particles in solution.[33]

Interestingly, we found that the interface strength of the same non-polar zinc/cristobalite interfaces is significantly enhanced once the siloxane rings are broken. However, since this requires to overcome a large energy barrier, it may not be feasible in normal conditions. In this respect, we have proposed surface pre-hydroxylation[35] or formation of interfacial ternary compounds[36,37] as possible routes for removing the surface reconstruction and enhancing adhesion.

One alternative path may rely on using interfacial buffers composed of more reactive metals. Indeed, in the superficially similar case of alumina/zinc interfaces, we have previously shown that early transition metal[38] or stainless steel[39] buffers can significantly enhance adhesion resulting in cohesive cleavage within the zinc deposit. However, the similarity between the two systems is limited. In contrast to silica surfaces, stoichiometric alumina surfaces do not undergo a reconstruction and therefore expose undercoordinated atoms which can readily bond to a reactive metal deposit.

Therefore, in order to shed more light on the microscopic mechanisms which drive the interaction at different metal/silica interfaces, as well as to explore the suitability of stainless steel buffers to improve adhesion at zinc/silica interfaces, in this paper we study the interaction of β-cristobalite with a series of transition metals (M) of different electronic and cohesive properties, with particular attention to the interaction between surface siloxane rings and different metallic species and its consequences for adhesion. As to cover a wide range of characteristics we have chosen metals from the beginning (Ti), the middle (Cr, Fe) and the end (Ni) of the 3*d* transition series, a choice that also includes the three components of stainless steel (Fe, Cr and Ni). Taking into account the similarity of results obtained for interfaces between Zn and the (001) and (111) surfaces of cristobalite,[34] in the following we restrict our analysis to the case of (001)-oriented interfaces under various oxygen conditions.

The paper is organized as follows. After presenting the computational approach in Sec. 2, in Sec. 3 we summarize the main results on the structural, electronic and adhesion properties of the interfaces. In Sec. 4 we discuss the similarities and differences between silica/metals and alumina/metals junctions and how they affect the use of stainless steel buffers to enhance adhesion properties, before summarizing our conclusions (Sec. 5).

2 Computational methods and settings

All calculations were performed within Density Functional Theory (DFT) as implemented in VASP (Vienna ab initio simulation package).[40,41] We have used a dispersion-corrected GGA exchange-correlation functional (optB86-vdW),[42–44] as we have found it to improve the description of adhesion characteristics at weakly interacting metal/oxide interfaces with respect to standard GGAs.[38,45] In particular dispersive interactions account for the majority of the adhesion energies between zinc and reconstructed silica surfaces.[34] The interaction of valence electrons with ionic cores is described within the projector augmented wave (PAW) method,[46,47] and the *p* semicore electrons of the transition metal atoms have been systematically treated explicitly. Since it has a relatively small effect on the energetic trends, we did not employ the GGA+U approach to correct the electronic structure of the transition metal atoms oxidized at interfaces[45]. The Kohn-Sham orbitals are developed on a plane-wave basis set with a cutoff energy of 400 eV, and we use a Γ-centered 6×6 Monkhorst-Pack grid. The self-consistent iterative solution of the electronic Hamiltonian is pursued until energy differences become less than 10^{-6} eV and atomic positions were relaxed until forces become smaller than 0.01 eV Å^{-1}. Periodic slab replicas were systematically separated by at least 10 Å of vacuum and we used dipole corrections to attenuate the effect of periodic boundary conditions in the direction normal to the slab surfaces.[40] Atomic charges are estimated with the partition scheme proposed by Bader,[48,49] and atomic configurations are plotted with VESTA.[50]

The relative stability of magnetic and non-magnetic solutions was systematically tested for transition metal surface and interfaces. As expected, ferromagnetic ground states were found for iron and nickel, and a non-magnetic state for titanium. For chromium, we find a non-magnetic ground state with the optB86-vdW functional, and the surface energy is $\sim$50% larger than the value measured in the liquid phase, consistently with previous DFT results.[51–53] An error cancellation can however be expected in adhesion and interface energies. To model silica surfaces we employ the I$\bar{4}$2d structural variant of β-cristobalite, following the results and discussion in Refs. 54 and 34.

Surface calculations In the present study we consider four (001)β-cristobalite surface terminations of different composition, atomic structure and polar character analyzed in detail in our previous work,[34] namely two non-polar stoichiometric ones and polar oxygen-lean and oxygen-rich (Fig. 1).

Following the convention of Ref. 34, we will label them according to their surface stoichiometry with respect to a neutral dipoleless repetitive bulk unit cell[55]: SiO (O-lean), D_2-SiO_2 and SiO_2 (stoichiometric), and SiO_3 (O-rich). In the case of the stoichiometric terminations, both dangling oxygen terminated (SiO_2) and reconstructed terminations which expose instead siloxane rings (D_2-SiO_2) are considered[34]. Non-stoichiometric terminations are polar, containing an excess of two electrons (O-lean) or two holes (O-rich) per surface unit cell which heal their polar character. For O-lean terminations, the excess electrons are localized on surface cations, which change their oxidation state from Si^{4+} to Si^{2+}. For O-rich terminations, the excess holes are localized on surface anions, which form O_2^{2-} peroxo surface groups.

In order to reduce the propagation of structural distortions and to improve the convergence with respect to slab thickness, we use asymmetric silica slabs with one bare and one fully hydroxylated termination, and fix the position of the sub-surface Si atoms at hydroxylated terminations. Although slabs composed of five SiO_2 layers are sufficient to converge surface energies to within 0.01 J/m^2, as convergence of the separation energies can be somewhat

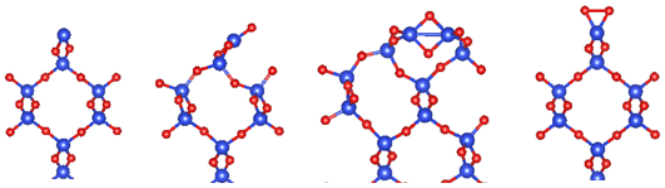

Fig. 1 Computational models of alternative terminations of the (001) surface of β-cristobalite. From left to right: oxygen-lean SiO, stoichiometric SiO_2 and D_2-SiO_2, and oxygen-rich SiO_3 terminations. Si and O atoms are represented by large blue and small red balls, respectively.

slower we use systematically nine SiO_2 layers.

The total surface energy of such non-stoichiometric asymmetric slab is equal to the sum of the surface energies of its bare σ_{SiO_x} and its hydroxylated σ_{SiOH} terminations:

$$\sigma_{SiO_x} + \sigma_{SiOH} = \frac{E^{a-slab} - E^{bulk}_{SiO_2} - nE_{H_2O} - \Delta N_O \mu_O}{S} \quad (1)$$

where E^{a-slab}, $E^{bulk}_{SiO_2}$, and E_{H_2O} are the total energies of the asymmetric slab, of bulk SiO_2, and of a free water molecule, respectively. ΔN_O gives the excess/deficiency of oxygen atoms in the slab with respect to the SiO_2 ($+nH_2O$) stoichiometry, μ_O is the oxygen chemical potential, and S is the surface unit cell area. Since the evaluation of σ_{SiO_x} requires the knowledge of σ_{SiOH}, the total energy E^{s-slab} of a symmetric stoichiometric cristobalite slab with both terminations equivalently hydroxylated is also calculated.

Table 1 Orientation and coincidence unit cells of the metal deposit used in interface calculations, calculated in-plane lattice parameters a and b (Å) and angles α, and lattice mismatch δa, δb with respect to the (1×1)-(001) surface unit cell of β-cristobalite ($a = b =$ 4.89 Å, α=90°).

Metal	unit cell	a, b (Å)	δa, δb (%)	α
Ti hcp	$(2\sqrt{2}\times\sqrt{2})$-$(11\bar{2}0)$	4.62, 5.04	-5.5, +3.1	90
Cr bcc	(2×2)-(110)	4.88, 4.88	-0.2, -0.2	109.5
Fe bcc	(2×2)-(110)	4.86, 4.86	-0.6, -0.6	109.5
Ni fcc	$(\sqrt{2}\times\sqrt{2})$-(001)	4.94, 4.94	+1.0, +1.0	90

The surface energies of non-stoichiometric terminations depend on the oxygen chemical potential μ_O, which we refer to the total energy of a free oxygen molecule E_{O_2}: $\mu_O = \frac{1}{2}E_{O_2} + \Delta\mu_O$. $\Delta\mu_O \sim 0.0$ eV corresponds to oxygen-rich conditions (condensation of oxygen molecules) and $\Delta\mu_O \sim -4.7$ eV to extremely oxygen-poor conditions (decomposition of bulk SiO_2).

Interface calculations The simulations of metal/SiO_2 interfaces make use of the same asymmetric SiO_2 slabs with metal films deposited on their bare terminations. Tab. 1 summarizes the orientations of the metal films and the interface coincidence cells used in the calculations, together with the corresponding interface mismatch for the lattice parameters and angle. We have systematically used deposits of 9 metal layers for Ni, Fe and Cr, and 12 layers for Ti slabs which have lower surface density. In order to minimize the interfacial strain, the lattice parameters and angles are fixed to the average between the values for the silica and metal surface unit cell. The most stable interface configurations are obtained from a series of independent optimizations, starting from various interface registries between the two lattices.

The interface strength is estimated from the separation energy:

$$E^{sep} = -(E_{SiO_x/metal} - E^{a-slab} - E_{metal})/S \quad (2)$$

where E_{metal/SiO_x}, E^{a-slab} and E_{metal} are the total energies of the metal/SiO_x heterostructure, of the isolated silica slab and of the metal one respectively (all with the same in-plane lattice parameters), and S is the surface of the average cell described above. The interface stability is estimated from the interface energy:

$$E^{int} = \sigma_{SiO_x} + \sigma_{metal} - E^{sep} \quad (3)$$

with σ_{SiO_x} and σ_{metal} being the surface energies of SiO_x and metal surfaces, respectively, computed using the average unit cell in order to be consistent with the separation energies.

In order to test the uncertainty created by our choice to deal with the lattice mismatch, we have performed a single reference calculation on a larger cell which provides a very good lattice matching. This was done for the SiO_2/Cr interface, as the Cr and Fe cells display the largest mismatch with respect to the cristobalite unit cell (19.5° difference between angles). To this end, we have used a SiO_2(001)-(3x4) || Cr(110)-$(5\sqrt{2}$x$5\sqrt{2})$ coincidence cell, where the $(\sqrt{2}$x$\sqrt{2})$ is referring to the rectangular Cr surface unit cell (see Fig. S1 in the Supplementary Information). With this choice, the two cells have the same angle and only a $+3\%$ and -3% mismatch in the lattice parameters. We obtain in this way a separation energy of 2.86 Jm^{-2}, to be compared to 3.02 Jm^{-2} obtained using the (1x1)-SiO_2 unit cell and average lattice parameters and angle (see section 3). We conclude that the the latter choice is sufficient to accommodate the interfacial strain and give accurate results within a margin of ∼0.15 Jm^{-2}.

3 Results

3.1 Interface structures

Fig. 2 shows the optimized structures of the metal deposits in contact with the stoichiometric and non-stoichiometric (001) terminations of β-cristobalite and highlights the interfacial M-O and M-Si bonds. The number of bonds per unit cell at each interface is summarized in Tab. 2 (the maximum length of M-Si bonds is set to 2.8 Å, the sum of the covalent radii of Si and the largest metal atoms). Some trends along the transition metal series are common to all interfaces. Interfaces with nickel and iron display very similar structures, resembling to a large degree a juxtaposition of the bare surfaces. Chromium and titanium interfaces show larger distortions of both metal and oxide lattices with the formation of additional M-O bonds.

Specifically, the characteristics of non-polar interfaces depend very strongly on the nature of the deposited metal. As will be discussed in Sec. 3.4, the M/D_2-SiO_2 configurations, involving intact interfacial siloxane rings, are systematically less stable than the M/SiO_2 ones, where these rings are broken. When relaxing the interface structure starting from a M/D_2-SiO_2 configuration, the siloxane rings are preserved for M=Fe,Ni, and a single M-O bond per reconstructed (2x1) surface cell is formed. However, the

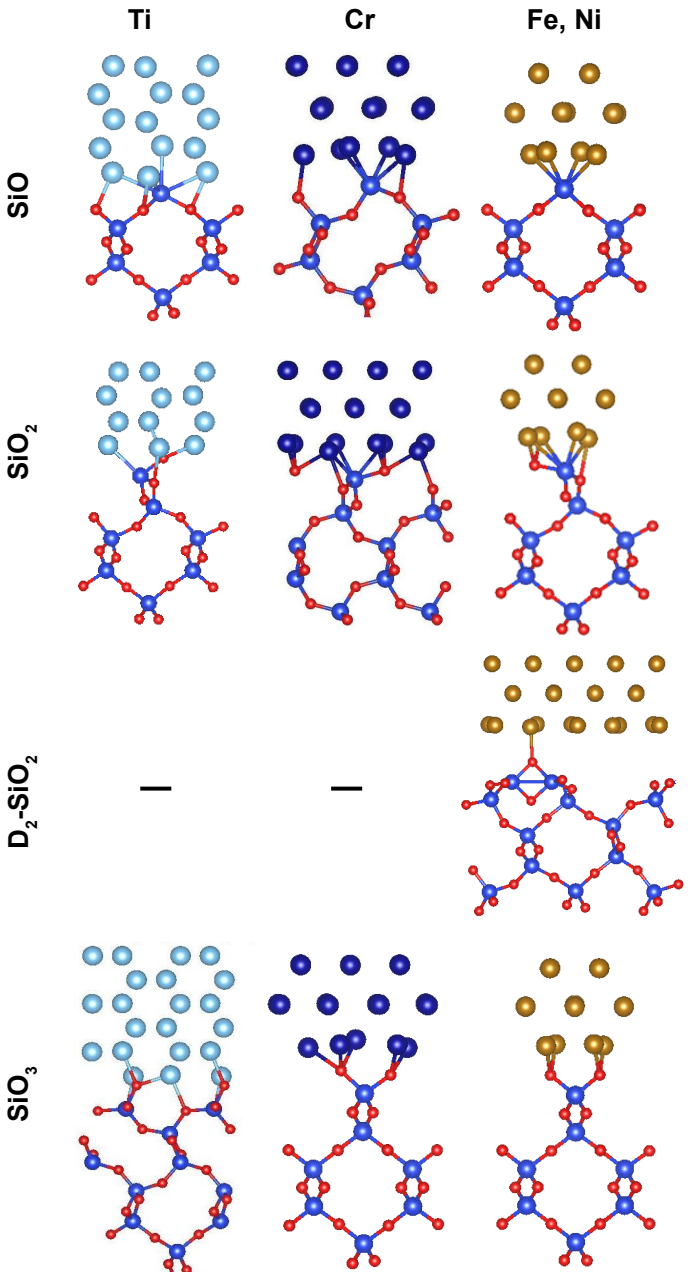

Fig. 2 Schematic representation of the optimized structures of metal/SiO_2(001) interfaces for Ti (left), Cr (middle), Ni and Fe (right), and different β-crystobalite surface terminations (top to bottom). Si and O atoms are shown with large blue and small red balls, respectively.

Table 2 Number of interfacial M-O and M-Si bonds per unit cell at silica/metal interfaces (the cutoff distance for defining a M-Si bond is set to 2.8 Å). The D_2-SiO_2 has double cell surface area with respect to the other terminations.

	Ti	Cr	Fe	Ni
M-O				
SiO	2	1	0	0
SiO_2	4	4	3	3
D_2-SiO_2	-	-	1	1
SiO_3	5	5	4	4
M-Si				
SiO	5	4	4	4
SiO_2	1	3	3	3

siloxane rings break spontaneously for M=Cr,Ti, and the interface relaxes to a M/SiO_2 configuration. The existence of metastable M/D_2-SiO_2 configurations for iron and nickel indicates that energy barriers prevent the interface siloxane rings from breaking, similarly to what was found for Zn/SiO_2 interfaces.[34] Conversely, the disappearance of the reconstruction when titanium and chromium are deposited is a signature of a much stronger metal/oxide interaction, consistently with the higher tendency of early transition metals to be oxidized. Once siloxane rings are broken, the M/SiO_2 interfaces display a smaller structural dependence on the metallic specie. The undercoordinated oxygen atoms at the cristobalite surface interact with the metal, forming two bonds with nickel and iron and three with chromium and titanium. Interestingly, in all cases a distortion of both metal and oxide lattices enables also a formation of one M-O bonds involving sub-surface oxygens. In addition, weaker M-Si bonds are formed in all cases (three for M=Cr, Fe, Ni and only one for Ti, owing to the less dense surface structure of the latter).

At the M/SiO interfaces, due to the absence of undercoordinated surface anions, the interfaces are dominated by M-Si bonds formed between the surface silicon atoms and the metal deposits. The number of M-Si bonds is essentially constant along the series (four per interface unit cell), but an additional such bond can be identified in the case of Ti, again due the different surface structure. We recall that only two M-Si bonds per interface unit cell are formed at the corresponding Zn/SiO interface[34]. Only in the cases of Cr and Ti, M-O bonds involving sub-surface oxygens are also formed.

For the oxygen-rich M/SiO_3 interfaces, in all cases the metal deposit forms bonds with the surface oxygens, breaking the peroxo groups present on the silica surface. The full coordination of silicon atoms prevents the formation of any M-Si bonds. A structural distortion allows the formation of an additional M-O bond for M=Cr,Ti. In the case of chromium, such distortion is concentrated in the metal deposit, while for titanium it occurs in the silica lattice. We note that, especially for the most electropositive metals, the excess oxygen at the interface could diffuse inside the metal deposit forming an interfacial oxide layer, depending on the energy barriers for breaking the Si-O bonds and for oxygen diffusion. Exploration of this kind of interface configurations is beyond the scope of the present work.

Table 3 Atomic Bader charges of interfacial silicon and oxygen atoms (Q_{Si} and Q_O respectively) and total charge of the metal deposits Q_M^{tot} (e) at the silica/metal interfaces. As a reference in bulk silica Q_{Si} = 3.18 e and Q_O = -1.59 e.

	Ti	Cr	Fe	Ni	Bare
SiO					
Q_{Si}	0.19	1.15	1.51	1.73	1.61
Q_M^{tot}	1.43	0.43	0.07	-0.18	-
SiO_2					
Q_{Si}	1.64	1.93	2.26	2.49	2.96
Q_O	-1.47	-1.36	-1.30	-1.28	-1.25
Q_M^{tot}	1.45	1.02	0.62	0.34	-
D_2-SiO_2					
Q_{Si} (x2)	-	-	3.15	3.15	3.17
Q_O (x2)	-	-	-1.62	-1.57	-1.56
Q_M^{tot}	-	-	0.12	0.06	-
SiO_3					
Q_{Si}	3.16	3.16	3.15	3.14	3.08
Q_O (x2)	-1.47	-1.40	-1.33	-1.27	-0.65
Q_M^{tot}	1.43	1.26	1.19	1.00	-

3.2 Electronic structure

The electronic characteristics of the series of interfaces (Bader charges in Tab. 3 and projected density of states shown in Fig. S2 in the Supplementary Information) corroborate the insight provided by their atomic structures. Independently of the interface polarity, the charge transfer Q_M^{tot} decreases along the transition metal series, with titanium transferring the largest amount of electrons to silica and nickel the smallest. This is consistent both with the variation of the number of interfacial M-O bonds and with the trends of electronegativity and electron affinity along the metal series (see Sec. 4). The charge accepted by the metal deposit is mostly localized in the interfacial layer and on the atoms which form M-O bonds, especially for Ti and Cr.

The smallest charge transfers occur at the M/D_2-SiO_2 interface (M=Fe, Ni). In this case the charges of the bare silica substrate are already close to their bulk values, and the very small variation upon depositing the metal, together with the very small degree of M-O hybridization visible in the DOS (see Fig. S2), confirm the weakness of the interaction. The M/SiO_2 interface displays significantly larger charge transfers, which are maximal for M=Ti and decrease along the series. The electrons transferred from the metal deposits are principally localized on surface cations, with oxygen atoms accommodating at most 15% of the transferred charge. Silicon charges Q_{Si} are in all cases smaller than those at the bare SiO_2 surface, and increase along the transition metal series concomitantly with decreasing charge transfers. The lowest value (for M=Ti) is only 55% of the one at the bare surface and close to the one at oxygen-poor surfaces, suggesting a Si^{2+} oxidation state.

The electronic structure at the oxygen-poor M/SiO interface shows significant similarities, despite the polarity resulting in the presence of Si^{2+} cations already on the bare surface. Only in the case of Ni the metal accepts a small fraction of the excess electrons localized on the surface Si^{2+}. For the other more electropositive metals, the direction of the electron transfer is from the metal to the oxide. The amount is negligible for iron, but becomes progressively larger for chromium and titanium, where direct M-O bonding is observed in both structures and projected density of states (see Fig. S2). Indeed, the silicon oxidation state approaches Si^{0+} for the Ti/SiO interface.

The picture is rather different for the M/SiO_3 interfaces. In this case, the breaking of the surface O_2^{2-} groups allows interfacial anions to accept additional electrons from the metal, which heals the surface polarity. Oxygens atoms approach the O^{2-} bulk-like oxidation state, with values of Bader charges very similar to those of the SiO_2 interfaces. Conversely, the cationic charges are unchanged and close to both bulk and surface values. This results in a value of interfacial charge transfer which is much less dependent on the specific metal deposit with respect to M/SiO and M/SiO_2 interfaces.

3.3 Separation energies

Separation energies obtained for the four interface configurations are summarized in Tab. 4.

The lowest values are obtained for the M/D_2-SiO_2 interfaces (M=Fe, Ni), confirming the picture inferred from the structural and electronic properties. Indeed, as previously observed for zinc deposits, if the fully coordinated siloxane rings are preserved at the interface the adhesion is extremely weak. Conversely, M/SiO_2 interfaces where the silica reconstruction is absent display moderate-to-strong adhesion strengths. Concerning non-stoichiometric interfaces, we find that the oxygen-rich ones (M/SiO_3), which have the largest number of metal-oxygen bonds, produce systematically the strongest metal-oxide interaction. Oxygen-lean interfaces (M/SiO) display moderate adhesion strengths despite the low number (Ti and Cr) or absence (Fe and Ni) of metal-oxygen bonds.

Table 4 (top) Separation energies E^{sep} (J/m^2) of metal/silica interfaces as a function of the metal and of the silica surface termination, and minimal separation energy at the oxygen-rich interfaces when considering metal decohesion (SiO_3+M, see text). The separation energy M/M within the metal (i.e. $2E^{surf}$) is reported for comparison. (bottom) Interface energies E^{int} for the SiO_2 and D_2-SiO_2 interfaces.

	Ti	Cr	Fe	Ni
Separation energies				
SiO	2.44	1.86	1.23	1.99
SiO_2	3.69	3.02	2.44	2.28
D_2-SiO_2	–	–	0.36	0.34
SiO_3	6.44	5.77	4.17	4.05
$SiO_3 + M$	3.90	4.08	2.71	3.47
M/M	4.27	7.28	5.54	5.34
Interface energies				
SiO_2	0.73	2.88	2.59	2.65
$D_2 - SiO_2$	-	-	3.38	3.35

The overall behavior of E^{sep} along the series of metals is qualitatively the same for M/SiO_2 and M/SiO_3 interfaces, despite the differences in structure and type of interface bonds. Indeed, the above discussed progressive decrease of the amplitude of interfacial structural and electronic interactions from titanium to nickel along the series is clearly reflected in a progressive decrease of

the interface strength. A similar trend is present also for M/SiO interfaces, with the exception of the Ni/SiO one which displays an higher separation energy than both Fe/SiO and Cr/SiO. This correlates very well with the charge transfer at the interface, as nickel is the only metal to accept electrons from the undercoordinated cations, screening the polarity of the oxygen-poor surface. Indeed, the lowest interface strength among M/SiO interfaces is obtained for iron, which has also the lowest interfacial charge transfer in absolute value.

Metal decohesion The strength of the silica/metal junction corresponds to the minimum separation energy within the multicomponent system. Metal decohesion can shift the preferred cleavage plane from the interface to a close-by position within the metal deposit, as we have shown for oxygen-rich silica/zinc interfaces.[34] Therefore, we have estimated to what extent the interfacial charge transfer and the partial metal ionization impact the bonding within the different metal deposits. In previous studies, this effect was found to be significant only at oxygen-rich interfaces[37], and the minimal separation energy was reached when a number of metal atoms close to that needed to compensate the surface polarity was left on the oxide surface.[34] Therefore, we have tested whether the separation energies decrease when one metal atom per O_2^{2-} group is left on the silica surface, breaking the peroxo group and compensating the surface polarity. As seen in Tab. 4, the separation energies are lower than both the ones obtained for interfacial M/SiO_3 cleavage and the ones obtained for cleavage within the metal deposit (i.e. twice the metal surface energy), pointing towards a degree of metal decohesion. The interface strength remains however relatively high and larger than the one of non-polar interfaces for all metals considered.

3.4 Interface energies

The interaction with the metal deposits strongly influences the stability of the different cristobalite terminations. The interface energies of stoichiometric interfaces, which are independent of the chemical potential, are reported in Tab. 4. In contrast to the case of bare silica surfaces, the M/D_2-SiO_2 configurations, involving intact interfacial siloxane rings, become less stable with respect to the M/SiO_2 ones, where the rings are broken, also for iron and nickel deposits, which do not induce ring breaking. This is explained by the very weak interaction across the D_2-SiO_2 interface, and specifically by the fact that only one weak M-O bond per (2x1) surface cell can be formed if the surface reconstruction is preserved. Polar terminations are stabilized in a wide range of oxygen chemical potentials (see Fig. S3 in the Supplemental Information). This effect results from the screening of surface polarity and from the formation of M-O bonds, as discussed above for the separation energies. Indeed, the Ti/SiO_3 and Cr/SiO_3 interfaces are stable over the widest range of chemical potentials, and the Ni/SiO interface is also substantially stabilized. We note however that non-polar interfaces will remain the most relevant when the metal is deposited on a bare silica surface.

The values of the M/SiO_2 interface energies, reported in Tab. 4, represent well the trends of interface stability along the metals series, as polar terminations behave similarly to non-polar ones in this respect (see Fig. S3 in the Supplementary Information). We recall that interface energies can be interpreted as a difference of surface and separation energies (Eq. 3). The interface energies for M=Cr,Fe,Ni are very similar, which arises from a compensation between the metal surface energies and the metal-oxide interaction. Conversely, the Ti/SiO_2 interface energy is very low, as titanium displays both the lowest surface energy and the strongest interaction with silica. In this respect, we note that titanium oxidizes in slightly more oxygen-poor conditions than silicon (see Sec. 4). The low values of interface energy, which become even negative for the Ti/SiO_3 interface in oxygen-rich conditions, may then reflect a preference of titanium for oxidizing if energy barriers for oxygen diffusion can be overcome.

4 Discussion

In the following, we first analyze how the trends of interfacial charge transfer are related to the electronegativities and oxygen affinities of the transition metals. We then discuss the similarities and differences between the interaction of silica and alumina stoichiometric surfaces with metal deposits. Finally, we analyze whether, similarly to alumina,[39] the presence of a multicomponent metallic buffer may enhance adhesion at zinc/silica interfaces.

4.1 Trends in interface charge transfer

As discussed in Sec. 3.2, the interfaces of all stoichiometries display a charge transfer towards the metal deposit which decreases along the transition metal series. The oxidation of the metal deposits is accompanied by a reduction of interface silicon cations. The trend along the metal series can be principally linked to the values of the metal electronegativity χ_M, or, alternatively, to the affinity towards oxygen quantified by the critical values of oxygen chemical potential above which metal oxidation is thermodynamically favored:

$$\Delta\mu_O^c = \Delta_f H^0 / N_O \quad (4)$$

where $\Delta_f H^0$ is the standard enthalpy of oxide formation at 298.15K[56,57] and N_O is the number of oxygen atoms per formula unit. We note that the $\Delta\mu_O^c$ values obtained from DFT formation energies are very similar to those deduced from the standard enthalpies of formation (see Fig. S4 in Suppl. Info.).

$\Delta\mu_O^c$ and χ_M have a similar behavior (see Fig. 3). Both increase along the transition metal series and decrease again for zinc (see Tab. 5), a trend which is mirrored in interfacial charge transfers. Specifically, the higher electronegativity of nickel compared to other metals explains why the charge transfer at the Ni/SiO interface has an opposite sign with respect to all other cases. Conversely, as titanium is the least electronegative metal and $\Delta\mu_O^c$ of titanium and silicon have similar values, a pronounced reduction of Si cations at interfaces with metallic Ti is indeed to be expected.

4.2 Comparison between M/SiO_2 and M/Al_2O_3 interfaces

The interaction between Al_2O_3(0001) surfaces and metal deposits is discussed in detail in Refs. 38,39,45. A typical alumina/metal interface structure is recalled in Fig. 4. The stoichiometric alumina surface is Al-terminated, but three subsurface oxygen atoms

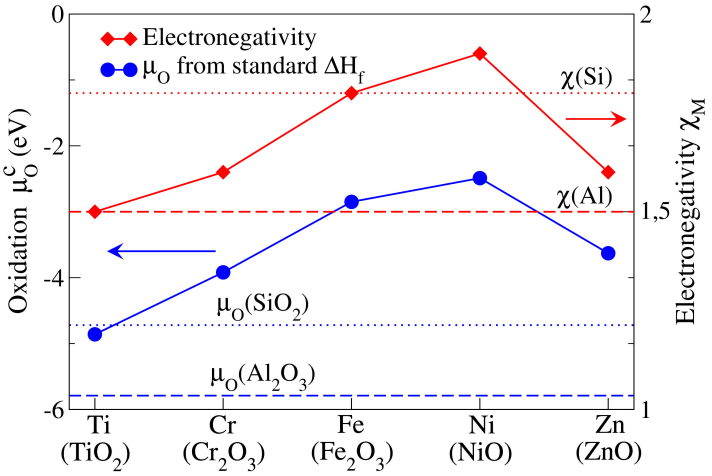

Fig. 3 Critical values of oxygen chemical potential $\Delta\mu_O^c$ at which oxidation of the metallic species considered in this study is thermodynamically favored, deduced from the experimental standard enthalpies of oxide formation ΔH_f(298.15 K) per oxygen atom [56,57] , and electronegativities χ_M of the same metals.

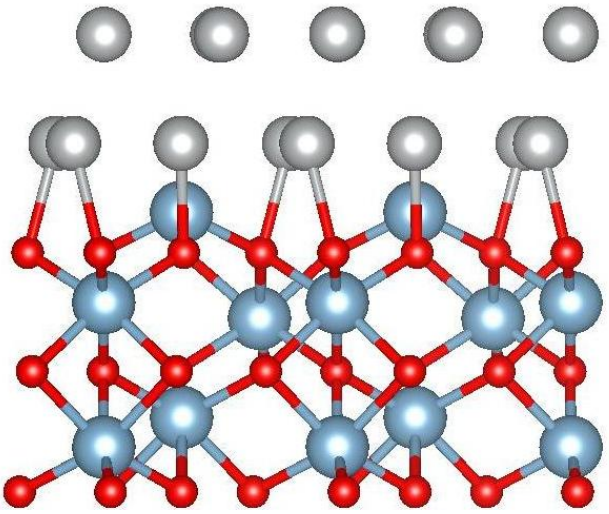

Fig. 4 Schematic representation of the Ni/Al_2O_3(001) interface (the structure of other M/Al_2O_3 interfaces is qualitatively similar). Aluminium, oxygen and nickel atoms are represented by large blue, small red and medium grey balls respectively.

per unit cell are undercoordinated and can form O-M bonds across the interface. In the following we compare the thermodynamically stable (i.e. non-reconstructed) stoichiometric interfaces of alumina and silica.

In Tab. 5 we summarize the most relevant structural and electronic properties of the two interfaces. The first factor that we consider is the number and length of interfacial M-O bonds. Three M-O bonds per unit cell are systematically formed across M/Al_2O_3 interfaces, while at M/SiO_2 interfaces three (for M=Fe, Ni, Zn) or four (for M= Ti, Cr) bonds are formed. At the same time, the surface area of the Al_2O_3 unit cell is $\sim$ 20% smaller, with the result that the bond density at M/Al_2O_3 is somewhat larger for late transition metals and somewhat lower for early transition metals with respect to M/SiO_2 interfaces. However, M-O bonds are systematically longer for M/Al_2O_3 interfaces, a characteristics which is particularly evident for the case of a zinc deposit. This is caused by the alumina surface structure, which is terminated by an Al cation. The steric repulsion causes the interfacial M-O bonds to be elongated and thus weaker. Note that for interfaces with silica, only the M-O bonds which involve subsurface oxygen atoms (one per unit cell, see Sec. 3) are significantly elongated.

The trends of the interfacial charge transfers along the metal series are similar for alumina and silica (Tab. 5, see also Sec. 3.2 and 4.1). The main difference between the two oxides is a smaller charge transfer at the interfaces involving alumina, particularly pronounced for late transition metals and less so for titanium. This is partially due to the structural differences described above. Indeed, longer and weaker M-O bonds at alumina interfaces result in lower charge transfer values. More importantly, the $\Delta\mu_O^c$ for oxide formation is significantly lower for alumina than for silica. Therefore, Al cations are less prone to be reduced at the interface, contributing to the smaller charge transfers. Zinc transfers a moderate amount of the electrons at the interface with SiO_2, as expected from the Zn oxygen affinity, but a negligible amount at the interface with Al_2O_3. This is a consequence of the particularly long Zn-O bond lengths at the latter interface, which prevent zinc oxidation.

The separation energies at the oxide/metal interfaces are compared in Fig. 5. The trend along the metal series is overall similar, with a decrease of the adhesion strength along the metal series (see also Sec. 3), but the adhesion energies for M/Al_2O_3 interfaces are lower by about 1 J m^{-2}. Two factors can rationalize this difference. The first is the different surface structure of the two oxides, which results in more elongated and weaker M-O bonds at alumina/metal contacts. The second is the lower electronegativity of Al, which contributes to a smaller interfacial charge transfer and metal/oxide interaction.

The same factors which cause the difference in separation energies affect the interface energies as well (Fig. 5), as interface energies can be obtained as a difference of surface and separation energies (Eq. 3). We recall here that the silica and alumina surface energies are 2.2 J m^{-2} and 1.9 J m^{-2}, respectively, and that the zinc surface energy is 0.6 J m^{-2}. The trend along the metal series is the same for silica and alumina, with relatively low E_{int} for Ti and Zn due chiefly to the low surface energies of the metals, and very similar E_{int} values for Cr, Fe and Ni which result from a compensation between separation and surface energies (see also Sec. 3.4). M/Al_2O_3 interface energies are higher by $\sim$ 0.5 Jm^{-2}, as a consequence of the lower separation energies at alumina interfaces.

4.3 Stainless steel buffers at the SiO_2/Zn interface

In the following, we will make use of the results discussed in the previous section in order to estimate whether stainless steel buffers can be used to improve the silica/zinc interface strength. We recall that stainless steel buffers, with a composition around 75%Fe, 12.5%Cr and 12.5%Ni, have been found to greatly increase the adhesion at the alumina/zinc interface.[39] For a non-oxidized buffer, the adhesion improvement resulted directly from

Table 5 Atomic charges of the oxide cations Q_{Si} and Q_{Al}, total charge of the metal deposits Q_M^{tot}, number N_{M-O} of metal-oxygen bonds per unit cell, and their length d_{M-O} at the non-polar M/SiO_2 and M/Al_2O_3 interfaces.

		Ti	Cr	Fe	Ni	Zn	Bare surf.
M/SiO_2	Q_{Si} (e)	1.64	1.93	2.26	2.49	2.31	2.96
	Q_M^{tot}(e)	1.45	1.02	0.62	0.34	0.71	
	N_{M-O}	4	4	3	3	2	
	d_{M-O}(Å)	1.96,2.06	1.97,2.02	1.95x2	1.94x2	1.97x2	
		2.14,2.25	2.13,2.2	2.28	2.18		
M/Al_2O_3	Q_{Al} (e)	1.15	1.93	2.07	2.22	2.26	2.41
	Q_M^{tot}(e)	1.19	0.42	0.19	0.08	0.09	
	N_{M-O}	3	3	3	3	3	
	d_{M-O}(Å)	2.27-2.44	2.06	2.06, 2.11	2.05x3	2.71x3	
			2.2x2	2.16			

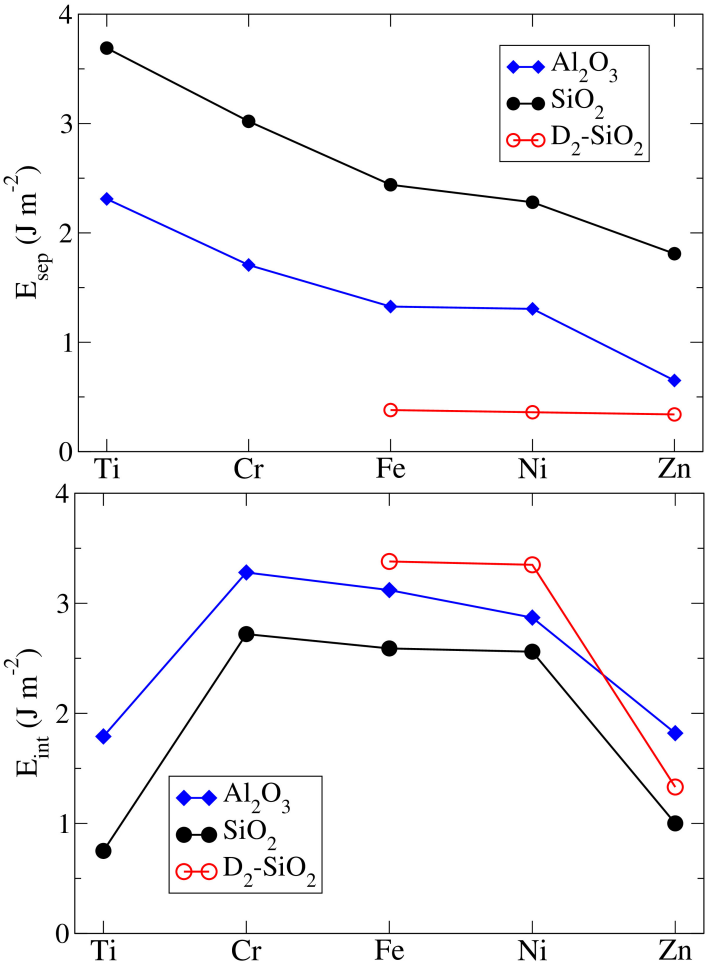

Fig. 5 Comparison of the separation energies (top) and interface energies (bottom) at non-polar M/SiO_2 and M/Al_2O_3 interfaces.

the high strength of the interfaces between transition metals (TMs) contained in steel, most importantly the predominant iron component, and both alumina and zinc. Notably, however, this improvement held also if the buffer was partially oxidized.[39] In this case, the strong adhesion relied on the segregation of transition metal oxides at the interface with alumina, and the resulting suppression of the weakly interacting oxide/zinc and moderately strong alumina/metal interfaces. We stress that in Ref. 39 the internal structure of the buffer was optimized by a Monte Carlo approach. Nevertheless, the qualitative results can be very well understood in terms of minimization of the sum of all interface energies across the oxide/stainless steel/zinc superstructure. Specifically, it was found that the metal/oxide interface energies are systematically larger than oxide/oxide ones, and metal/metal interface energies are zero or negative owing to the tendency of metals to alloy. As a consequence, the buffer arranged itself to have a single metal/oxide interface, causing the segregation of transition metal oxides near alumina. In analyzing the SiO_2/stainless steel/Zn superstructure, we will therefore also base our reasoning on the relative values of metal/metal, oxide/oxide and oxide/metal interface energies.

In oxygen-lean conditions, none of the components of the buffer are oxidized. If the silica surface is reconstructed, it has a high interface energy with iron and nickel but a lower one with chromium (see Fig. 5). Chromium has then a thermodynamic preference for segregating at the interfaces, and promote the breaking of surface siloxane rings. Once the siloxane rings are broken, the transition metals have similar interface energies with silica, as in the case of alumina. The buffer is then expected to have the same internal structure, with a prevalence of iron and chromium at the interface with silica and iron and nickel at the interface with zinc. As silica/metal separation energies are larger than alumina/metal ones (see Fig. 5), the steel buffer will perform as well or better for enhancing zinc adhesion on silica compared to alumina.

In intermediate oxygen conditions, chromium and possibly iron oxides will form in the buffer. In this case there are two possible scenarios, shown schematically in Fig. 6. The first possibility is that the transition metal oxides (TMOs) segregate near the silica. The second is that the TMOs are found between two metals, either in the central part of the steel buffer or between the transition

SiO_2	Transition Metal Oxide	Transition Metal	Metal (TM or Zn)	Zn

SiO_2	Transition Metal	Transition Metal Oxide	Metal (TM or Zn)	Zn

Fig. 6 Schematic representation of two possible ordering of a stainless steel buffer at an oxide/zinc interface.

metals (TMs) and zinc. The total interface energy for the two buffer configurations is:

$$E^1_{buf} = E^{SiO_2/TMO}_{int} + E^{TMO/TM}_{int} + E^{TM/M}_{int} + E^{M/Zn}_{int}$$
$$E^2_{buf} = E^{SiO_2/TM}_{int} + E^{TM/TMO}_{int} + E^{TMO/M}_{int} + E^{M/Zn}_{int} \quad (5)$$

and which configuration is stable depends on the sign of the energy difference:

$$\Delta E_{buf} = E^{SiO_2/TMO}_{int} + E^{TM/M}_{int} - E^{SiO_2/TM}_{int} - E^{TMO/M}_{int} \quad (6)$$

We recall here that the interface energies between TMOs and metals $E^{TMO/M}_{int}$ are in the range 0.5—1.5 J m^{-2} and $E^{TM/M}_{int} \leq 0$,[39] while $E^{SiO_2/TM}_{int}$ is in the range 2.6—2.9 J m^{-2}. Therefore $\Delta E_{buf} \leq E^{SiO_2/TMO}_{int} - 3.1$ J m^{-2}. We have no quantitative estimation of $E^{SiO_2/TMO}_{int}$, but considering the low values normally found for oxide/oxide interface energies[37,39] (often in the range 0.5—1.0 J m^{-2}) we expect ΔE_{buf} to be significantly negative. As a consequence, the segregation of TMOs near silica will be thermodynamically favored. As oxide/oxide interfaces have strong adhesion properties,[28,37,39] and the remainder of the buffer will behave as in the case of alumina substrates, formation of chromium or iron oxides is not expected to degrade the performance of the multicomponent buffer.

As a final point, we examine if mixing of silica with transition metal oxides, resulting in the formation of ternary oxides, could influence the performance of the buffer. Chromium silicates are not normally found,[58] and indeed chromia does not mix with silica on the surface of oxidized steels,[13] but iron silicate Fe_2SiO_4 is a common ternary oxide in the form of the mineral fayalite.[59] However, the critical oxygen chemical potential for the formation of fayalite from iron and silica is only slightly lower (by 0.1 eV) than the μ^c_O value for Fe_2O_3 formation. Therefore, chromium will be the first transition metal to oxidize independently of the presence of silica, and chromium oxide segregation at the interface will prevent iron silicate formation.

5 Conclusions

In summary, relying on DFT calculations, we report a thorough and systematic fundamental study of polar and non-polar interfaces between β-cristobalite and several 3d transition metals and provide a full set of corresponding state-of-the-art structural, electronic, and energetic interface characteristics. We find a progressive decrease of the metal/silica separation energy along the transition metal series from Ti to Ni, independently of the precise interface stoichiometry and structural characteristics. The trend is to be principally linked to the behavior of metal electronegativity and of its affinity towards oxygen, which drive a decrease of electron transfers along the series.

We find that, at non-polar interfaces, whether the silica surface reconstruction, exposing fully saturated siloxane rings, remains intact at the interface is crucial for adhesion strength. The metal deposit induces in all cases a stability reversal between the unreconstructed SiO_2 and the reconstructed $D_2 - SiO_2$ configurations, and makes the interfacial siloxane rings thermodynamically unstable. However, late transition metals (Ni and Fe) do not induce a spontaneous ring breaking, leading to very weak adhesion similarly to zinc. At interfaces with Cr and Ti deposits, conversely, the reconstruction is lifted without energy barriers, resulting in moderate-to-strong interface strength. At interfaces where the reconstruction is lifted, the resulting trends in interface and adhesion energies are similar to those found at alumina/metal interfaces, but with a stronger interaction which can be linked principally to the difference in interface structures and to the lower electronegativity of aluminium.

On the basis of the results obtained, we estimate that early transition metal or stainless steel buffers can successfully improve adhesion of anticorrosive zinc coatings on oxidized Si-rich steel grades, of crucial importance in steel-making and automotive industries. More generally, the insight in behavior of metal/silica interfaces gained in the present study may provide a useful basis in other fields of applications, such as electronics, catalysis or nanotechnology.

Acknowledgments

The authors are grateful to Jacques Jupille, Rémi Lazzari, Lucie Gaouyat and Daniel Chaleix for many fruitful discussions. J. Baima and H.-L. T. Le acknowledge post-doctoral grants from ArcelorMittal Maizières Research.

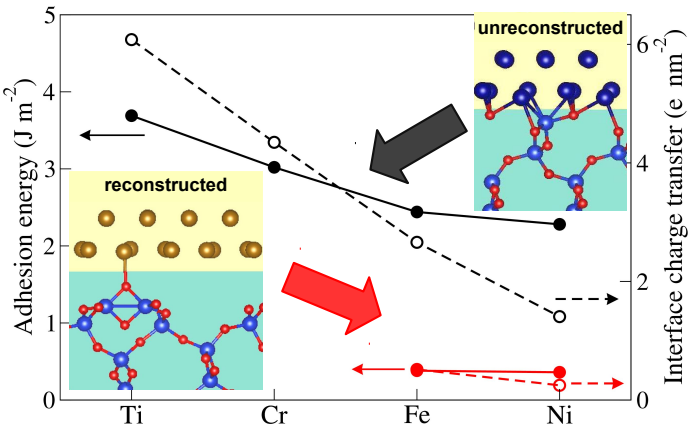

Figure: TOC image

Notes and references

1 C. T. Campbell, *Surface Science Reports*, 1997, **27**, 1–111.

2 Q. Fu and T. Wagner, *Surface Science Reports*, 2007, **62**, 431–498.

3 A. Picone, M. Riva, A. Brambilla, A. Calloni, G. Bussetti, M. Finazzi, F. Ciccacci and L. Duò, *Surface Science Reports*, 2016, **71**, 32 – 76.

4 M. Englisch, A. Jentys and J. A. Lercher, *Journal of Catalysis*, 1997, **166**, 25–35.

5 C. Xu, G. Chen, Y. Zhao, P. Liu, X. Duan, L. Gu, G. Fu, Y. Yuan and N. Zheng, *Nature communications*, 2018, **9**, 1–10.

6 J. ZhuChen, J. Gao, P. R. Probus, W. Liu, X. Wu, E. C. Wegener, A. J. Kropf, D. Zemlyanov, G. Zhang, X. Yang *et al.*, *Catalysis Science & Technology*, 2020.

7 Y. Lu, Y. Yin, Z.-Y. Li and Y. Xia, *Nano Letters*, 2002, **2**, 785–788.

8 K. Xu, J.-X. Wang, X.-L. Kang and J.-F. Chen, *Materials Letters*, 2009, **63**, 31–33.

9 Z. Bian and S. Kawi, *ChemCatChem*, 2018, **10**, 320–328.

10 D. K. Yoon, A. Kumar, D.-G. Lee, J. Lee, T. Kwon, J. Choi, T. Jin, J. H. Shim and I. S. Lee, *Nano letters*, 2019, **19**, 3627–3633.

11 T. W. Hansen, A. T. DeLaRiva, S. R. Challa and A. K. Datye, *Accounts of chemical research*, 2013, **46**, 1720–1730.

12 P. Tabib Zadeh Adibi, V. P. Zhdanov, C. Langhammer and H. GroÌĹnbeck, *The Journal of Physical Chemistry C*, 2015, **119**, 989–996.

13 A. Huntz, V. Bague, G. Beauplé, C. Haut, C. Sévérac, P. Lecour, X. Longaygue and F. Ropital, *Applied Surface Science*, 2003, **207**, 255–275.

14 P. Drillet, Z. Zermout, D. Bouleau, J.-M. Mataigne and S. Claessens, *Rev. Metall.-Cah. Inf. Tech.*, 2004, **10**, 831–837.

15 H.-T. Jiang, W. Ding, D. Tang and W. Huang, *J. Iron and Steel Research*, 2012, **19**, 29–36.

16 W. Wang, M. Li, C. He, X. Wei, D. Wang and H. Dub, *Materials and Design*, 2013, **47**, 510–521.

17 A. Mertens, E. M. Bellhouse and J. R. McDermid, *Materials Science & Engineering A*, 2014, **608**, 249–257.

18 *Advanced high strength sheet steels*, ed. N. Fonstein, Springer Int. Publishing, Switzerland, 1st edn, 2015.

19 B. Hu, H. Luo, F. Yang and H. Dong, *J. Mater. Sci. Technol.*, 2017, **33**, 1457–1464.

20 A. R. Marder, *Prog. Mater. Sci.*, 2000, **45**, 191–271.

21 G. Bordier and C. Noguera, *Phys. Rev. B*, 1991, **44**, 6361–6371.

22 J. Goniakowski and C. Noguera, *Interface Science*, 2004, **12**, 93–103.

23 J. Goniakowski, C. Mottet and C. Noguera, *physica status solidi (b)*, 2006, **243**, 2516–2532.

24 G. Pacchioni, *Physical Chemistry Chemical Physics*, 2013, **15**, 1737–1757.

25 K. Nagao, J. B. Neaton and N. W. Ashcroft, *Phys. Rev. B*, 2003, **68**, 125403.

26 T.-R. Shan, B. D. Devine, S. R. Phillpot and S. B. Sinnott, *Phys. Rev. B*, 2011, **83**, 115327.

27 A. Ngandjong, C. Mottet and J. Puibasset, *The Journal of Physical Chemistry C*, 2017, **121**, 3615–3622.

28 E. A. A. Jarvis and E. A. Carter, *J. Am. Ceram. Soc.*, 2003, **86**, 373–386.

29 B. Magyari-Kope, S. Park, L. Colombo, Y. Nishi and K. Cho, *J. Appl. Phys.*, 2009, **105**, 013711.

30 C. S. Ewing, G. Veser, J. J. McCarthy, J. K. Johnson and D. S. Lambrecht, *The Journal of Physical Chemistry C*, 2015, **119**, 19934–19940.

31 P. N. Plessow, R. S. Sanchez-Carrera, L. Li, M. Rieger, S. Sauer, A. Schaefer and F. Abild-Pedersen, *J. Phys. Chem. C*, 2016, **120**, 10340–10350.

32 N. Vakula, G. Kuramshina and Y. A. Pentin, *Russian Journal of Physical Chemistry A*, 2013, **87**, 296–302.

33 H. Balout, N. Tarrat, J. Puibasset, S. Ispas, C. Bonafos and M. Benoit, *ACS Applied Nano Materials*, 2019, **2**, 5179–5189.

34 H.-L. T. Le, J. Goniakowski, C. Noguera, A. Koltsov and J.-M. Mataigne, *Phys. Chem. Chem. Phys.*, 2018, **20**, 6254–6263.

35 H.-L. T. Le, J. Goniakowski, C. Noguera, A. Koltsov and J.-M. Mataigne, *Physical Chemistry Chemical Physics*, 2018, **20**, 15581–15588.

36 J. Baima, J. Goniakowski, C. Noguera, A. Koltsov and J.-M. Mataigne, *Phys. Chem. Chem. Phys.*, 2019, **21**, 13287–13295.

37 J. Baima, J. Goniakowski, C. Noguera, A. Koltsov and J.-M. Mataigne, *The Journal of Physical Chemistry C*, 0, **0**, null.

38 H.-L. T. Le, J. Goniakowski, C. Noguera, A. Koltsov and J.-M. Mataigne, *J. Phys. Chem. C*, 2016, **120**, 9836–9844.

39 H.-L. T. Le, J. Goniakowski, C. Noguera, A. Koltsov and J.-M. Mataigne, *The Journal of Physical Chemistry C*, 2017, **121**, 25143–25151.

40 G. Kresse and J. Furthmuller, *Phys. Rev. B*, 1996, **54**, 11169–11186.

41 G. Kresse and J. Hafner, *Phys. Rev. B*, 1993, **47**, 558–561.

42 M. Dion, H. Rydberg, E. Schroder, D. C. Langreth and B. I. Lundqvist, *Phys. Rev. Lett.*, 2004, **92**, 246401.

43 J. Klimes, D. R. Bowler and A. Michaelides, *J. Phys.: Cond. Matt.*, 2010, **22**, 022201.

44 J. Klimes, D. R. Bowler and A. Michaelides, *Phys. Rev. B*, 2011, **83**, 195131.

45 R. Cavallotti, H.-L. T. Le, J. Goniakowski, R. Lazzari, J. Jupille, A. Koltsov and D. Loison, *Phys. Chem. Chem. Phys.*, 2016, **18**, 3032–3039.

46 P. E. Blöchl, *Phys. Rev. B*, 1994, **50**, 17953–17979.

47 G. Kresse and J. Joubert, *Phys. Rev. B*, 1999, **59**, 1758–1775.

48 R. F. W. Bader, *Chem. Rev.*, 1991, **91**, Chem. Rev.

49 G. Henkelman, A. Arnaldsson and H. Jonsson, *Comput. Mater. Sci.*, 2006, **36**, 354–360.

50 K. Momma and F. Izumi, *J. Appl. Crystallogr.*, 2011, **41**, 1272–1276.

51 R. Hafner, D. Spišák, R. Lorenz and J. Hafner, *Physical Review B*, 2002, **65**, 184432.

52 T. Ossowski and A. Kiejna, *Surface science*, 2008, **602**, 517–524.
53 R. Soulairol, C.-C. Fu and C. Barreteau, *Physical Review B*, 2011, **84**, 155402.
54 T. Demuth, Y. Jeanvoine, J. Hafner and J. G. Angyan, *J. Phys.: Condens. Matter*, 1999, **11**, 3833.
55 J. Goniakowski, F. Finocchi and C. Noguera, *Rep. Prog. Phys.*, 2008, **71**, 016501.
56 M. W. C. Jr., *J. Phys. Chem. Ref. Data*, 1998, **Monograph 9**, 1–1951.
57 J. D. Cox, D. D. Wagman and V. A. Medvedev, *CODATA Key Values for Thermodynamics*, Hemisphere Publishing Corp., New York, 1984.
58 F. Seifert and K. Langer, *Contributions to Mineralogy and Petrology*, 1970, **28**, 9–18.
59 J. R. Smyth, *American Mineralogist: Journal of Earth and Planetary Materials*, 1975, **60**, 1092–1097.